HRLT: A high-resolution (1 day, 1 km) and long-term (1961–2019) gridded dataset for surface temperature and precipitation across China

Rongzhu Qin, Zeyu Zhao, Jia Xu, Jian-Sheng Ye, Feng-min Li, Feng Zhang[*]

State Key Laboratory of **Herbage Improvement and** Grassland Agro-ecosystems, College of Ecology, Lanzhou University, Lanzhou, 730000, China

[*] Corresponding author: Feng Zhang

Tel.: +86 13919274617

Fax: +86 09318912561

E-mail: zhangfeng@lzu.edu.cn

Address: College of Ecology, Lanzhou University, 222 Tian Shui South Road, Lanzhou, 730000, China

Abstract

Accurate long-term temperature and precipitation estimates at high spatial and temporal resolutions are vital for a wide variety of climatological studies. We have produced a new, publicly available, daily, gridded maximum temperature, minimum temperature, and precipitation dataset for China with a high spatial resolution of 1 km and over a long-term period (1961 to 2019). It has been named the HRLT and the dataset is publicly available at https://doi.org/10.1594/PANGAEA.941329 (Qin and Zhang, 2022). In this study, the daily gridded data were interpolated using comprehensive statistical analyses, which included machine learning **methods**, the generalized additive model, and thin plate splines. It **was**is based on the $0.5° \times 0.5°$ grid**ed** dataset from the China Meteorological Administration, together with covariates for elevation, aspect, slope, topographic wetness index, latitude, and longitude. The accuracy of the HRLT daily dataset was assessed using observation data from meteorological stations across China. The maximum and minimum temperature estimates were more accurate than the precipitation estimates. For maximum temperature, the mean absolute error (MAE), root mean square error (RMSE), Pearson's correlation coefficient (Cor), coefficient of determination after adjustment (R^2), and Nash-Sutcliffe modeling efficiency (NSE) were 1.07 °C, 1.62 °C, 0.99, 0.98, and 0.98, respectively. For minimum temperature, the MAE, RMSE, Cor, R^2, and NSE were 1.08 °C, 1.53 °C, 0.99, 0.99, and 0.99, respectively. For precipitation, the MAE, RMSE, Cor, R^2, and NSE were 1.30 mm, 4.78 mm, 0.84, 0.71, and 0.70, respectively. The accuracy of the HRLT was compared to those of the other three existing datasets and its accuracy was either greater than the others, especially for precipitation, or comparable in accuracy, but with higher spatial resolution or over a longer time period. In summary, the HRLT dataset, which has a high spatial resolution, covers a longer period of time and has reliable accuracy, is suitable for future

45 ~~environmental analyses, especially the effects of extreme weather~~.

1 Introduction

47   Climate change has led to an increase in the frequency and severity of extreme temperature

48 and precipitation events (Myhre et al., 2019), and these events have affected vegetation growth (Xu

49 et al., 2019), especially crop growth (Rao et al., 2015; Li et al., 2019b; Lu et al., 2018; Lobell et al.,

50 2011; Lesk et al., 2016). Thus, long-term and accurate daily maximum temperature, minimum

51 temperature, and precipitation data are important when attempting to reveal the mechanism

52 underlying the effects of extreme climate on plants, predicting disasters (such as drought, frost, and

53 floods), and for agricultural and forestry management. Although the meteorological observation

54 network makes better use of the data from meteorological stations (Merino et al., 2014; Yang et al.,

55 2014), there is a tradeoff between large spatial scale and the high density of stations in the

56 meteorological observation network. Moreover, the installation and maintenance of meteorological

57 stations are challenging in harsh areas (Hartl et al., 2020). Daily and gridded meteorological datasets

58 are also essential inputs for many models related to terrestrial, hydrological, and ecological systems

59 (Iizumi et al., 2017; Wang et al., 2018; Zhang et al., 2018; Lee et al., 2019). High-resolution, long-

60 term, and accurate gridded datasets can help improve the performance of these models.

61   Researchers have previously used interpolation methods, such as inverse distance weighting,

62 kriging, and regression analysis, to produce grid**ed** meteorological data (Brinckmann et al., 2016;

63 Herrera et al., 2019; Schamm et al., 2014). However, the accuracy of these interpolation results is

64 limited by the density of the meteorological stations. In recent years, artificial intelligence, machine

65 learning methods, such as random forest (Chen et al., 2021; Sekulić et al., 2021); artificial neural

66 networks (Sadeghi et al., 2021), and support vector machines (He et al., 2021) have been gradually

67 and widely applied to meteorological data estimation. Therefore, comprehensive statistical analyses

68 using machine learning and traditional interpolation, such as thin-plate-smoothing splines, are

69 feasible and reliable methods that can be used to estimate meteorological data.

70 At present, only a few research institutes in China are developing meteorological datasets for

71 temperature and precipitation with high spatial and temporal resolutions. Among them, Beijing

72 Normal University has produced meteorological datasets for 1958–2010 with a resolution of 1 km,

73 but the latest data is not available (Li et al., 2014). The China Meteorological Administration is also

74 developing the CMA Land Data Assimilation System product (Shi et al., 2011) and Tsinghua

75 University has published a driving dataset from 1979 to 2018 with a resolution of 0.1° over China

76 (He et al., 2020).

77 We present a new high-resolution daily gridded maximum temperature, minimum temperature,

78 and precipitation dataset for China (HRLT) with a spatial resolution of 1×1 km for the period 1961

79 to 2019. We created the HRLT dataset using comprehensive statistical analyses, which included

80 machine learning, the generalized additive model and thin plate splines. It uses the $0.5° \times 0.5°$ grided

81 dataset from the China Meteorological Administration (CMA) as input data together with other

82 covariates, including elevation, aspect, slope, topographic wetness index (TWI), latitude, and

83 longitude. The dataset was created in three steps: (1) preparation of input data and covariates; (2)

84 the creation of the gridded dataset using comprehensive statistical analyses; and (3) an evaluation

85 of the accuracy of the gridded dataset and accuracy comparison with other three exiting products

86 that use meteorological station data.

2 Data

2.1 The CMA dataset and meteorological stations data

The CMA dataset, which includes the daily surface temperature 0.5° × 0.5° grid**ed** dataset (http://101.200.76.197/data/cdcdetail/dataCode/SURF_CLI_CHN_TEM_DAY_GRID_0.5.html) and the daily precipitation 0.5° × 0.5° grid**ed** dataset for China (V2.0) (http://101.200.76.197/data/cdcdetail/dataCode/SURF_CLI_CHN_PRE_DAY_GRID_0.5.html **https://data.cma.cn/, last access: 15 September, 2022**), was obtained from the China Meteorological Data Service Centre and was used as the basic input data. The researchers also reported daily precipitation 0.5° × 0.5° grid**ed** dataset during 1961-2010 from CAM dataset (Zhao and Zhu, 2015). The daily dataset of surface climatological data for China (V3.0) (http://101.200.76.197/data/cdcdetail/dataCode/SURF_CLI_CHN_MUL_DAY_V3.0.html **https://data.cma.cn/, last access: 15 September, 2022**), which includes 699 meteorological stations, was also obtained from the China Meteorological Data Service Centre and was used to evaluate the new dataset (Fig. 1).

2.2 Topographic data

The basic topographic data, including elevation, flow direction, and flow accumulation with a 30 second (approximately 1 km) resolution, were obtained from the HydroSHEDS database. More detailed information can be found at these links: http://www.worldwildlife.org/hydrosheds **(last access: 15 September, 2022)** for general information and http://hydrosheds.cr.usgs.gov **(last access: 15 September, 2022)** for data download and technical information. The "Aspect" and "Slope" option of the Spatial Analyst Tools in ArcGIS10.6 were used to calculate aspect and slope.

108 The specific catchment area (SCA) was calculated based on flow direction and flow accumulation.

109 The TWI is formulated as **follow:**~~TWI = ln(SCA / tan(Slope)).~~

$$TWI = ln(\frac{SCA}{\tan(Slope)}) \tag{1}$$

110 **where TWI and SCA is topographic wetness index and specific catchment area,**

111 **respectively.**

2.3 Other datasets

113 **We used observed data from meteorological stations (Fig. 1) to evaluate our dataset and**

114 **the existing three daily datasets, then the accuracy of the existing three daily datasets was**

115 **compared to that of our dataset, respectively.**~~Three temperature and precipitation products with~~

116 ~~daily resolutions were evaluated using observed meteorological stations data and the evaluation~~

117 ~~results were compared to the HRLT dataset in this study~~. The China Meteorological

118 Administration Land Data Assimilation System (CLDAS) version 2 dataset was provided by the

119 China Meteorological Data Service Centre (https://data.cma.cn/ **, last access: 15 September,**

120 **2022**) for 2017 to 2019 with a 0.0625° (approximately 7.5 km) spatial resolution and a 1 day

121 temporal resolution. The China Meteorological Forcing Dataset (CMFD) (He et al., 2020; Yang

122 and He, 2019) was obtained from the National Tibetan Plateau Third Pole Environment Data

123 Center (https://data.tpdc.ac.cn/ **, last access: 15 September, 2022**) for 1979 to 2018 with a spatial

124 resolution of 0.1° (approximately 12 km) and a temporal resolution of 1 day. The historical dataset

125 relating to the Inter-Sectoral Impact Model Intercomparison Project (ISIMIP3a) was obtained

126 from the web (https://data.isimip.org/ **, last access: 15 September, 2022**) for 1961 to 2016 with a

127 spatial resolution of 0.5° (approximately 60 km) and a temporal resolution of 1 day. The daily

128   maximum temperature, minimum temperature, and precipitation data in the CLDAS and

129   ISIMIP3a were used for evaluation and comparison. The daily average temperature and

130   precipitation data from the CMFD was also used for evaluation and comparison.

3 Methods

131

3.1 The input data and covariates

132

133   In this study, the input data (dependent variable) was the daily 0.5° × 0.5° CMA dataset, which

134   includes daily maximum temperature, minimum temperature and precipitation. Other covariates

135   (independent variables) included elevation, aspect, slope, TWI (with a spatial resolution of 1 km),

136   latitude, and longitude.

3.2 The interpolation scheme

137

138   As shown in Figure 2, the different combinations of six algorithms, which are the boosted

139   regression trees (BRT), random forests (RF), neural networks (NN), multivariate adaptive

140   regression splines (MAR), support vector machines (SVM) and the generalized additive model

141   (GAM), to predict the input data. Firstly, through k-fold cross validation (k = 10), the input data was

142   was randomly divided into 10 sub-training datasets and sub-testing datasets. Each algorithm runs in

143   a loop through all the sub-training sets and calculates the residuals from the sub-testing sets. The

144   residuals obtained in each loop are retained. The residual of each algorithm is assigned a weight of

145   0-1 and summed up, and the ensemble of models that has the lowest residual sum is chosen. After

146   determining the best ensemble of models, surface results were interpolated using the best ensemble

147   of models, input data and covariates. The thin-plate-smoothing splines (TPS) is used to correct

148   residual error from the ensemble of models. Therefore, residuals of the ensemble are calculated from

149 the input data and these values are interpolated using TPS. Surface results from the ensemble add

150 residuals from the thin-plate-smoothing splines to get the surface result of final model. Compare R^2

151 of surface result from the ensemble and final model, and retain the surface result with higher R^2.

3.3 The **interpolation** methods

153 The introduction of individual algorithm (method) and the implementations for model training

154 (R packages and functions) of that is as follows. After the model training, the function 'predict' in

155 R package 'raster' used to **implemented** spatial interpolation for BRT, RF, NN, MAR, SVM and

156 GAM model, and the function 'interpolate' in R package 'raster' used to spatial interpolation for

157 TPS. More details on R packages and functions could refer the web

158 (https://www.rdocumentation.org/ **, last access: 15 September, 2022**).

3.3.1 The BRT model

160 As a powerful tool for exploratory regression analysis, BRT is a combination of two techniques:

161 decision trees and boosting method (Elith et al., 2008). The BRT can automatically detect the best

162 fit and is robust to missing values and outliers, therefore, BRT now widely used in ~~Remote~~ **remote**

163 sensing, species distribution and meteorological interpolation (Pouteau et al., 2011; Appelhans et

164 al., 2015; Froeschke and Froeschke, 2011). There are two important parameters in BRT, (1) the tree

165 complexity (TC): this controls the number of splits in each tree. (2) learning rate (LR): this

166 determines the contribution of each tree to the growth model. The smaller value of LR, the more

167 trees will be built. These two parameters together determine the number of trees required for the

168 best prediction in order to find the combination of parameters that leads to the least prediction error.

169 The function 'gbm.step' in R package 'dismo' for the BRT implementation. The ~~the~~ tree complexity

170 was set at 5, the learning rate was set at 0.001. In addition, the 'bag.fraction', which specifies the

171   proportion of data to be selected at each step, was set at 0.5 and other parameters are default values

172   in 'gbm.step'.

3.3.2 The RF model

174   Like BRT, the main technology of RF also includes decision trees, however, the way in which

175   the data to build the trees is selected is different (boosting method for BRT, bagging method for RF).

176   For regression analysis, the bagging method, which take a random subset of all data for each new

177   tree that is built, makes the final output based on average of multiple trees (Breiman, 2001). As one

178   of the most accurate algorithms, RF has been used widely for predicting spatio-temporal variables,

179   such as temperature and precipitation (He et al., 2016; Mital et al., 2020; Webb et al., 2016). The

180   function 'randomForest' in R package 'randomForest' for the RF implementation. The importance

181   was set TRUE, and other parameters are default values in 'randomForest'.

3.3.3 The NN model

183   As a powerful set of tools for solving problems in pattern recognition, data processing, and

184   non-linear control (Bishop, 1994), the NN consists of a large number of nodes and connections and

185   it includes input layer, hidden layer and output layer (Lek and Guégan, 1999). Information from

186   each node in the input layer is fed to the hidden layer. Connections between input layer nodes and

187   hidden layer nodes can all be given specific weights according to their importance. The connection

188   between the hidden layer and the output layer is also weighted, so the output is the result of the

189   weighted sum of the hidden nodes. Information transfer between hidden layer and output layer

190   through transfer function. Since the 1980s, the NN has been used in a number of fields, such as

191   prediction for meteorological variables (Snell et al., 2000; Lek and Guégan, 1999; Tang et al., 2020).

192   The function 'nnet' in R package 'nnet' for the NN implementation. The number of units in the

193   hidden layer (size) was set 10, the transfer function is linear for the output layer (linout was set

194   TRUE), the maximum number of iterations (maxit) was set 10000, and other parameters are default

195   values in 'nnet'.

3.3.4 The MAR model

197   The MAR is an extension of linear model, which can build multiple linear regression models

198   within the range of predictive variable values by partitioning data (Friedman, 1991; Friedman and

199   Roosen, 1995). The MAR consists of two steps: firstly, it creates a set of so-called basis functions.

200   In this process, the range of predictive variable values is divided into several groups. For each group,

201   separate linear regression was modeled. Secondly, MAR estimates a least square model with its

202   basis function as the independent variable. Overfitting is avoided by iterating to remove the basis

203   functions that contribute least to the model fitting. The MAR works well with a large number of

204   predictor variables, automatically detects interactions between variables and is robust to outliers,

205   therefore, studies has done on downscaling or predicting meteorological data using MAR (Panda et

206   al., 2022; Li et al., 2019a; Zawadzka et al., 2020). The function 'earth' in R package 'earth' for the

207   MAR implementation. Use linear model to estimate standard deviation as a function of the predicted

208   response (varmod.method = 'lm'). The nfold was set 10, the ncross was set 30, and other parameters

209   are default values in 'earth'.

3.3.5 The SVM model

211   The SVM is also one of the machine learning supervised algorithms and mainly deals with the

212   ideas of classification and regression (Vapnik, 1999; Vapnik, 1991; Brereton and Lloyd, 2010). The

213   SVM is well supported by mathematical theory and can use kernel tricks to efficiently process non-

214   linear data. With the development of SVM, it also has been widely used in the regression and

215   prediction of meteorological variables (Belaid and Mellit, 2016; Chen et al., 2010; Tripathi et al.,

216   2006). In this study, the function 'ksvm' in R package 'kernlab' for the SVM implementation and

217   all parameters are default values in 'ksvm'.

218   **3.3.6 The GAM model**

219   The GAM is an extension of the generalized linear model (GLM). Like GLM, GAM consists

220   of three important components: the probability distribution of the dependent variable, the linear

221   predictor and the link function, however, in GAM, the coefficient of the independent variable in the

222   linear is replaced by a sum of smooth functions (Hastie and Tibshirani, 2017; Liu, 2008). Because

223   the GAM can deal with nonlinear and non-monotone relationships between dependent and

224   independent variables, it has been used to predict and interpolate meteorological data (Hjort et al.,

225   2016; Burnett and Anderson, 2019; Aalto et al., 2013). The function 'gam' in R package 'mgcv' for

226   the GAM implementation and all parameters are default values in 'gam'.

227   **3.3.7 The TPS method**

228   As a traditional interpolation method, the TPS has been widely used to spatially interpolate

229   surface climate data (Gong et al., 2022; Hancock and Hutchinson, 2006; Risk and James, 2022). In

230   this study, it used to correct residual error from the ensemble of models. The function 'Tps' in R

231   package 'fields' for the TPS implementation. The matrix of independent variables consists latitude

232   and longitude, the vector of dependent variables is residual error in the combinations of above

233   algorithms, and other parameters are default values in 'Tps'.

234   **3.4 The interpolation implementation**

235   A complete operation was constructed per day per variable, so there were 64647 operations

236   (21549 days × 3 variables) from January 1, 1961 to December 31, 2019 for maximum temperature,

237 minimum temperature and precipitation. A complete operation for a day per variable requires a

238 Central Processing Unit core, 18 G of operating memory, and 2 hours of time. In order to shorten

239 the running time, we carried out parallel computing on a supercomputer platform. Spatial

240 interpolation work was executed by R version 4.0.2 (R Core Team, 2018) and the R package

241 "machisplin" (Brown, 2019) was referenced to achieve it.

3.5 Evaluation metrics

243   The mean absolute error (MAE), root mean square error (RMSE), Pearson's correlation

244 coefficient (Cor), coefficient of determination after adjustment (R^2), and Nash-Sutcliffe modeling

245 efficiency (NSE) were used to evaluate the interpolation results. Pearson's correlation coefficient

246 was used to evaluate the correlation between the simulated and observed values and the other

247 metrics are defined separately as follows:

$$MAE = \frac{1}{n}\sum_{i=1}^{n} | S_i - O_i| \tag{2}$$

$$RMSE = \sqrt{\frac{1}{n}\sum_{i=1}^{n}(S_i - O_i)^2} \tag{3}$$

$$R^2 = 1 - (1 - \frac{\sum_{i=1}^{n}(S_i - \bar{O})^2}{\sum_{i=1}^{n}(O_i - \bar{O})^2})\frac{(n-1)}{(n-k-1)} \tag{4}$$

$$NSE = 1 - \frac{\sum_{i=1}^{n}(S_i - O_i)^2}{\sum_{i=1}^{n}(O_i - \bar{O})^2} \tag{5}$$

248 where S_i and O_i are the model predicted and the experimentally observed values, respectively;

249 $\bar{O}$ is the mean of the observed values; n is the number of observations; and k is the value of the

250 independent variable. High Cor, R^2, and NSE values, and small RMSE and MAE values indicate

251 the strength of agreement between the predicted and observed values.

4 Results and discussion

4.1 Validation of temperature and precipitation

The spatial interpolation results, including daily maximum temperature, minimum temperature, and precipitation, were validated using meteorological station data. The results of the validation showed that the daily maximum and minimum temperatures were highly accurate (Fig. 3 and Table 1). The fitting slopes between the simulated and observed values were both close to 1 and the coefficients of determination after adjustment were 0.98 and 0.99, respectively, for daily maximum and minimum temperature (Figs. 3a, b). As shown in Table 1, the MAE was 1.07 °C and 1.08 °C, and the RMSE was 1.62 °C and 1.53 °C for daily maximum and minimum temperatures, respectively. In addition, the Cor and NSE values were close to 1 for both the daily maximum and minimum temperatures. Daily precipitation was less accurate than temperature with an R^2 of 0.71 (Fig. 3c), which was mainly caused by underestimating high daily precipitation. However, most of the points were concentrated in the low daily precipitation section. Furthermore, the MAE and RMSE for daily precipitation were 1.30 mm and 4.78 mm, respectively; the Cor between the simulated and observed daily precipitation was 0.84, and the NSE was 0.70 (Table 1).

The interpolation accuracy shows spatial differences (Fig. 4). The R^2 values of the daily maximum and minimum temperatures in southwest China were less than 0.94 and lower than those for other regions (Figs. 4a, c). The mean absolute errors for the daily maximum and minimum temperature ranges at most meteorological stations were less than 1 °C. However, there were some meteorological stations with mean absolute errors of more than 2 °C and these were evenly distributed across China (Figs. 4b, d). The R^2 value for daily precipitation at most meteorological

273 stations was greater than 0.7 and the MAE decreased from south to north across China (Figs. 4e, f).

274 **For precipitation where the R^2 map (Fig. 4e) shows a west-east gradient in the scores that is**

275 **different from the north-south gradient in the MAE map (Fig. 4f). There are fewer**

276 **meteorological observation stations in the western region than in the eastern region, which**

277 **may lead to the subtle east-west gradient of the R^2 value for daily precipitation. The obvious**

278 **north-south gradient for MAE of daily precipitation could be caused by the rainfall frequency**

279 **(Fig. 4f, Fig. 5), the MAE of monthly precipitation in China from other study showed a similar**

280 **pattern (Peng et al., 2019). Rainfall frequency above light rainfall, which is defined as a daily**

281 **rainfall from 0 to 4 mm (Alpert et al., 2002), is strongly correlated with the MAE of daily**

282 **precipitation (illustration in Fig. 5), so that the MAE of daily precipitation in the southern**

283 **region with higher rainfall frequency is larger than that in the northern region with lower**

284 **rainfall frequency.**

285   The meteorological stations were divided into the middle and lower reaches of the Yangtze

286 River (MLYR), North China (NC), Northeast China (NEC), Northwest China (NWC), South China

287 (SC), and Southwest China (SWC) (Fig. 1) according to their diverse geographic and climatic

288 conditions and administrative areas **(Qin, et al., 2022)**. The **cumulative distribution**

289 **functions**density distribution curve trend **of difference between the estimated and observed**

290 **values**for the simulated value and the observed value was always similar for daily maximum

291 temperature, minimum temperature, and precipitation in the six regions**, as well as in whole China**.

292 The daily maximum and minimum temperatures were all underestimated in the MLYR, NEC, NWC,

293 SC, and SWC**(Fig. 6a). The**, and the daily minimum temperatures were all underestimated in the

294 MLYR, **NC,** NWC, SC, and SWC (Fig. ~~5~~**6b**). For both daily maximum and minimum temperatures,

295 the lowest **average** difference between the simulated and observed ~~average~~ values occurred in **NC**

296 **and** NEC, while the greatest difference occurred in SWC (**Figs. 6a,b**~~Fig. 5~~). Except in the NWC

297 region, the **average difference between simulated and observed values**~~simulated average~~ for

298 daily precipitation was **less than 0 mm**~~lower than the observed average~~ in the other regions **(Fig.**

299 **6c)**. The largest **averages** difference between simulated and observed ~~averages~~ for daily

300 precipitation occurred in the SC region, with a value of 0.~~5~~**49** mm (Fig. ~~5~~**6c**). **Across whole China,**

301 **the average difference between simulated and observed values for daily maximum**

302 **temperature, minimum temperature, and precipitation was 0.36 °C, 0.30 °C and 0.12 mm,**

303 **respectively.**

304 ~~Figure 6 shows that the average diurnal variation values for daily temperature and precipitation~~

305 ~~based on the meteorological station data were almost the same as our estimations. Compared to the~~

306 ~~observations from the meteorological stations, the average values for daily maximum temperature~~

307 ~~decreased from 17.79 °C to 17.44 °C (1.9%) and the average values for daily minimum temperature~~

308 ~~decreased from 7.24 °C to 6.94 °C (4.1%) after interpolation, between 1961 and 2019 (Figs. 6a, b).~~

309 ~~The maximum values for daily maximum and minimum temperature measured by the~~

310 ~~meteorological stations were 33.35 °C and 22.24 °C, and the minimum values for those were −4.710 °C~~

311 ~~and −14.54 °C, respectively. After interpolation, these corresponding values became 33.23 °C and~~

312 ~~22.45 °C, −5.06 °C and −15.01 °C, respectively. Compared to the observations from meteorological~~

313 ~~stations, the average values for daily precipitation decreased from 2.43 mm to 2.31 mm (4.9 %) after~~

314 ~~interpolation, between 1961 and 2019 (Fig. 6c).~~

4.2 Temporal and spatial distributions of temperature and precipitation

The results showed that detailed spatial changes in temperature and precipitation over time could be obtained (Fig. 7). For example, the increase in annual average values (both maximum temperature and minimum temperature) were obvious over the Tibetan Plateau from 1965 to 2010 (Figs. 7a–h, the d1 and h1 subregions). In addition, compared with other years, the annual average daily minimum temperature clearly increased in some areas of NWC (Figs. 7e–h, the h2 and h3 subregions) and MLYR (Figs. 7e–h, the h4 subregion) in 2010. The most significant annual precipitation changes occurred in NEC (Figs. 7i–l, the l1 subregion) between 1965 and 2010.

The distributions of annual average daily maximum and minimum temperatures and annual precipitation across the six regions of China in 1965, 1980, 1995, and 2010 were analyzed (Fig. 8). Compared with other years, the areas with smaller values for annual average daily maximum temperature (less than 0) and annual average daily minimum temperature (less than −10) in SWC and NWC decreased in 2010 (Figs. 8a1, 8a2, 8b1, 8b2). These areas are mainly distributed on the Qinghai-Tibet Plateau, which has seen a large increase in temperature over the past few decades. The density distribution peak for the annual average daily maximum and minimum temperatures in NEC moved to the right from 1965 to 1995, but moved to the left in 2010 (Figs. 8a3, 8b3). The mean annual average daily minimum temperature in 2010 was higher in the MLYR, NC, and SC than in the other three years (Figs. 8b4–6). There was an increase in mean annual precipitation in the northern part of China over the period 1965–2010 (Figs. 8c2–4). It increased from 335 mm to 415 mm across NWC (Fig. 8c2), from 487 mm to 593 mm across NEC (Fig. 8c3), and from 531 mm to 654 mm across NC (Fig. 8c4). In the MLYR, there were more areas with annual precipitation

336   of less than 1000 mm, and areas with an annual precipitation of more than 2000 mm increased in

337   1995 and 2010 compared 1965 and 1980 (Fig. 8c5). Similarly, compared with other years, there

338   were more areas with annual precipitation of less than 1000 mm and more than 2000 mm in SC in

339   2010 (Fig. 8c6).

4.3 Accuracy comparison with other products

341   The performances of the CMFD, CLDAS and ISIMIP3a generated daily temperatures and

342   precipitations were evaluated against observations from all the meteorological stations and

343   compared their performance with that of our dataset (Figs. 9–11; Tables 2–4). The fitting slopes

344   between the simulated and observed daily temperature values were always close to 1 for all datasets

345   (Figs. 9a–c; Figs. 10a–d; Figs. 11a–d). The R^2 for the CMFD daily average temperature was

346   slightly smaller than that for daily minimum temperature in our dataset (Figs. 9b, c), but was equal

347   to our data set for daily maximum temperature (Figs. 9a, c). The Cor and NSE for the CMFD daily

348   average temperature were also similar to our estimated daily maximum and minimum temperatures

349   (Table 2). By contrast, the MAE and RMSE for the CMFD daily average temperature were 1.12 ℃

350   and 1.64 ℃, respectively, which were greater than for our estimated daily maximum and minimum

351   temperatures (Table 2). The MAEs of daily maximum and minimum temperature for our dataset

352   were 1.07 ℃ and 1.08 ℃ respectively; and the RMSEs of daily maximum and minimum

353   temperature for our dataset were 1.63 ℃ and 1.54 ℃, respectively, between 1979 and 2018 (Table

354   2). The R^2, Cor, NSE, MAE, and RMSE for the CLDAS daily maximum temperatures were 0.91,

355   0.95, 0.90, 2.54 ℃, and 3.63 ℃, respectively. Accuracy clearly improved for our daily maximum

356   temperature, and the corresponding metrics were 0.98, 0.99, 0.98, 1.10 ℃, and 1.73 ℃ (Figs. 10a,

357 b; Table 3). The MAE and RMSE for the CLDAS daily minimum temperature were clearly higher

358 than our estimates for daily minimum temperature, and the R^2, Cor, and NSE for daily minimum

359 temperature in our dataset were higher than those for the CLDAS daily minimum temperature (Figs.

360 10c, d; Table 3), thus indicating that the accuracy of our daily minimum temperature estimates was

361 superior to that of the CLDAS daily minimum temperature product. Compared with the ISIMIP3a,

362 the R^2, Cor, and NSE of daily maximum and minimum temperature in our dataset are always higher

363 and the MAE and RMSE of these are always smaller (Figs. 11 a–d; Table 4).

364   The R^2 value for our estimated daily precipitation clearly improved compared to the other

365 three datasets, especially the ISIMIP3a and CLDAS dataset (Figs. 9d, e; Figs. 10e, f; Figs. 11e, f).

366 The Cor and NSE for the CMFD daily precipitation were obviously smaller than those for our

367 dataset, and the RMSE for CMFD daily precipitation were greater than those for our dataset (Table

368 2). During 2017–2019, the Cor, NSE, MAE, and RMSE for our estimated daily precipitation were

369 0.84, 0.70, 1.42 mm, and 4.93 mm, respectively, and the corresponding values for the CLDAS daily

370 precipitation changed to 0.58, 0.28, 2.36 mm, and 7.67 mm, respectively (Table 3). During 1961–

371 2016, the Cor, NSE, MAE, and RMSE for our estimated daily precipitation were 0.84, 0.70, 1.30

372 mm, and 4.78 mm, respectively, and the corresponding values for the ISIMIP3a daily precipitation

373 changed to 0.48, 0.14, 2.75 mm, and 8.10 mm, respectively (Table 4). Thus, the daily precipitation

374 accuracy of our dataset was generally higher than that of CMFD, CLDAS and ISIMIP3a.

375 5 Data availability

376   The HRLT dataset includes daily maximum temperature, minimum temperature, and

377 precipitation at a 1 km spatial resolution across China from January 1961 to December 2019. The

378 datasets are publicly available in NetCDF format at https://doi.org/10.1594/PANGAEA.941329

379 (Qin and Zhang, 2022).

6 Conclusions

The result of this study is a high-resolution (1 km) daily gridded maximum temperature, minimum temperature and precipitation dataset across China for the long-term (1961–2019) (HRLT). The HRLT dataset shows an overall high correlation with the observations from meteorological stations for daily maximum and minimum temperatures (R^2 was 0.98 and 0.99, respectively; Cor were both 0.99; NSE was 0.98 and 0.99, respectively) and the errors were smaller (MAE was 1.07 ℃ and 1.08 ℃, respectively; RMSE was 1.62 ℃ and 1.53 ℃, respectively). Although the HRLT dataset showed that the daily precipitation accuracy was lower than the daily temperature accuracy (R^2, Cor, NSE, MAE, and RMSE were 0.71, 0.84, 0.70, 1.30 mm, and 4.78 mm, respectively), the daily precipitation data in the HRLT dataset were more accurate and had a finer spatial resolution compared to the other three existing datasets (CMFD, CLDAS and ISIMIP3a). Furthermore, the accuracies for daily maximum and minimum temperatures and precipitation were lower in the southwestern part of China, probably because of the complex topography in that area compared to other areas. Calculation and interpolation by subregions may solve this problem in future studies. The use of satellite data as an input covariate in future studies will further improve the accuracy of the HRLT dataset, especially for precipitation. The HRLT dataset will help identify future extreme climatic events and can be also used to improve process-based models for prediction, adaptation, and mitigation strategies.

Author contributions

Rongzhu Qin and Feng Zhang calculated the dataset, analyzed the results, and wrote the manuscript; all other authors reviewed and revised the manuscript.

Competing interests

The authors declare that they have no conflict of interest.

Acknowledgements

This study was supported by the Second Tibetan Plateau Scientific Expedition and Research (Grant No. 2019QZKK0305), National Natural Science Foundation of China (Grant No. 32071550), and the "111" Programme (BP0719040). We thank the Supercomputing Center of Lanzhou University for providing the computing requirements for this study. We are also grateful to the China Meteorological Data Service Centre, National Tibetan Plateau Third Pole Environment Data Center, Potsdam Institute for Climate Impact Research and the International Institute for Applied Systems Analysis for contributing datasets to the study. We are also thanking Dr. Marianne Rehage from PANGAEA for processing and publishing the dataset.

References

Aalto, J., Pirinen, P., Heikkinen, J., and Venäläinen, A.: Spatial interpolation of monthly climate data for Finland: comparing the performance of kriging and generalized additive models, Theor Appl Climatol, 112, 99-111, https://doi.org/10.1007/s00704-012-0716-9, 2013.

Alpert, P., T. Ben‑Gai, A. Baharad, Y. Benjamini, D. Yekutieli, M. Colacino, L. Diodato et al. The paradoxical increase of Mediterranean extreme daily rainfall in spite of decrease in total values, Geophysical research letters 29(11):31-1, https://doi.org/10.1029/2001GL013554, 2002.

Appelhans, T., Mwangomo, E., Hardy, D. R., Hemp, A., and Nauss, T.: Evaluating machine learning approaches for the interpolation of monthly air temperature at Mt. Kilimanjaro, Tanzania, Spatial Statistics, 14, 91-113, https://doi.org/10.1016/j.spasta.2015.05.008, 2015.

Belaid, S. and Mellit, A.: Prediction of daily and mean monthly global solar radiation using support

vector machine in an arid climate, Energy Conversion and Management, 118, 105-118, https://doi.org/10.1016/j.enconman.2016.03.082, 2016.

Bishop, C. M.: Neural networks and their applications, Review of scientific instruments, 65, 1803-1832, https://doi.org/10.1063/1.1144830, 1994.

Breiman, L.: Random forests, Machine learning, 45, 5-32, 2001.

Brereton, R. G. and Lloyd, G. R.: Support Vector Machines for classification and regression, Analyst, 135, 230-267, https://doi.org/10.1039/B918972F, 2010.

Brinckmann, S., Krähenmann, S., and Bissolli, P.: High-resolution daily gridded data sets of air temperature and wind speed for Europe, Earth Syst. Sci. Data, 8, 491-516, https://doi.org/10.5194/essd-8-491-2016, 2016.

Interpolation of noisy multi-variate data using machine learning ensembling: https://github.com/jasonleebrown/machisplin, last

Burnett, J. D. and Anderson, P. D.: Using generalized additive models for interpolating microclimate in dry-site ponderosa pine forests, Agricultural and Forest Meteorology, 279, 107668, https://doi.org/10.1016/j.agrformet.2019.107668, 2019.

Chen, S.-T., Yu, P.-S., and Tang, Y.-H.: Statistical downscaling of daily precipitation using support vector machines and multivariate analysis, J Hydrol, 385, 13-22, https://doi.org/10.1016/j.jhydrol.2010.01.021, 2010.

Chen, Y., Liang, S., Ma, H., Li, B., He, T., and Wang, Q.: An all-sky 1 km daily land surface air temperature product over mainland China for 2003–2019 from MODIS and ancillary data, Earth Syst. Sci. Data, 13, 4241-4261, https://doi.org/10.5194/essd-13-4241-2021, 2021.

Elith, J., Leathwick, J. R., and Hastie, T.: A working guide to boosted regression trees, J Anim Ecol, 77, 802-813, https://doi.org/10.1111/j.1365-2656.2008.01390.x, 2008.

Friedman, J. H.: Multivariate adaptive regression splines, The annals of statistics, 19, 1-67, https://doi.org/10.1214/aos/1176347963, 1991.

Friedman, J. H. and Roosen, C. B.: An introduction to multivariate adaptive regression splines, **3,192-217,** https://doi.org/10.1177/096228029500400303, 1995.

Froeschke, J. T. and Froeschke, B. F.: Spatio-temporal predictive model based on environmental factors for juvenile spotted seatrout in Texas estuaries using boosted regression trees, Fisheries Research, 111, 131-138, https://doi.org/10.1016/j.fishres.2011.07.008, 2011.

Gong, H., Liu, H., Xiang, X., Jiao, F., Cao, L., and Xu, X.: 1km Monthly Precipitation and Temperatures Dataset for China from 1952 to 2019 based on a Brand-New and High-Quality Baseline Climatology Surface, Earth Syst. Sci. Data Discuss., 2022, 1-30, 10.5194/essd-2022-45, 2022.

Hancock, P. A. and Hutchinson, M. F.: Spatial interpolation of large climate data sets using bivariate thin plate smoothing splines, Environmental Modelling & Software, 21, 1684-1694, https://doi.org/10.1016/j.envsoft.2005.08.005, 2006.

Hartl, L., Stuefer, M., Saito, T., and Okura, Y.: History and Data Records of the Automatic Weather Station on Denali Pass (5715 m), 1990–2007, Journal of Applied Meteorology and Climatology, 59, 2113-2127, https://doi.org/10.1175/jamc-d-20-0082.1, 2020.

Hastie, T. J. and Tibshirani, R. J.: Generalized additive models, Routledge2017.

He, J., Yang, K., Tang, W., Lu, H., Qin, J., Chen, Y., and Li, X.: The first high-resolution meteorological forcing dataset for land process studies over China, Scientific Data, 7, 25, https://doi.org/10.1038/s41597-020-0369-y, 2020.

He, Q., Wang, M., Liu, K., Li, K., and Jiang, Z.: GPRChinaTemp1km: a high-resolution monthly air temperature dataset for China (1951–2020) based on machine learning, Earth Syst. Sci. Data Discuss., 2021, 1-29, https://doi.org/10.5194/essd-2021-267, 2021.

He, X., Chaney, N. W., Schleiss, M., and Sheffield, J.: Spatial downscaling of precipitation using adaptable random forests, Water Resources Research, 52, 8217-8237, https://doi.org/10.1002/2016WR019034, 2016.

Herrera, S., Cardoso, R. M., Soares, P. M., Espírito-Santo, F., Viterbo, P., and Gutiérrez, J. M.: Iberia01: a new gridded dataset of daily precipitation and temperatures over Iberia, Earth Syst. Sci. Data, 11, 1947-1956, https://doi.org/10.5194/essd-11-1947-2019, 2019.

Hjort, J., Suomi, J., and Käyhkö, J.: Extreme urban–rural temperatures in the coastal city of Turku, Finland: Quantification and visualization based on a generalized additive model, Science of the Total Environment, 569, 507-517, https://doi.org/10.1016/j.scitotenv.2016.06.136, 2016.

Iizumi, T., Furuya, J., Shen, Z., Kim, W., Okada, M., Fujimori, S., Hasegawa, T., and Nishimori, M.: Responses of crop yield growth to global temperature and socioeconomic changes, Sci Rep-Uk, 7, 7800, https://doi.org/10.1038/s41598-017-08214-4, 2017.

Lee, M.-H., Im, E.-S., and Bae, D.-H.: Impact of the spatial variability of daily precipitation on hydrological projections: A comparison of GCM- and RCM-driven cases in the Han River basin, Korea, Hydrological Processes, 33, 2240-2257, https://doi.org/10.1002/hyp.13469, 2019.

Lek, S. and Guégan, J. F.: Artificial neural networks as a tool in ecological modelling, an introduction, Ecol Model, 120, 65-73, https://doi.org/10.1016/S0304-3800(99)00092-7, 1999.

Lesk, C., Rowhani, P., and Ramankutty, N.: Influence of extreme weather disasters on global crop production, Nature, 529, 84-87, https://doi.org/10.1038/nature16467, 2016.

Li, D. H. W., Chen, W., Li, S., and Lou, S.: Estimation of hourly global solar radiation using Multivariate Adaptive Regression Spline (MARS) – A case study of Hong Kong, Energy, 186, 115857, https://doi.org/10.1016/j.energy.2019.115857, 2019a.

Li, T., Zheng, X., Dai, Y., Yang, C., Chen, Z., Zhang, S., Wu, G., Wang, Z., Huang, C., Shen, Y., and Liao, R.: Mapping near-surface air temperature, pressure, relative humidity and wind speed over Mainland China with high spatiotemporal resolution, Advances in Atmospheric Sciences, 31, 1127-1135, https://doi.org/10.1007/s00376-014-3190-8, 2014.

Li, Y., Guan, K., Schnitkey, G. D., DeLucia, E., and Peng, B.: Excessive rainfall leads to maize yield loss of a comparable magnitude to extreme drought in the United States, Global Change Biology, 25, 2325-2337, https://doi.org/10.1111/gcb.14628, 2019b.

Liu, H.: Generalized additive model, Department of Mathematics and Statistics University of Minnesota Duluth: Duluth, MN, USA, 55812, 2008.

Lobell, D. B., Schlenker, W., and Costa-Roberts, J.: Climate Trends and Global Crop Production Since 1980, Science, 333, 616-620, https://doi.org/doi:10.1126/science.1204531, 2011.

Lu, Y., Hu, H., Li, C., and Tian, F.: Increasing compound events of extreme hot and dry days during growing seasons of wheat and maize in China, Scientific Reports, 8, 16700, https://doi.org/10.1038/s41598-018-34215-y, 2018.

Merino, A., Guerrero-Higueras, A. M., López, L., Gascón, E., Sánchez, J. L., Lorente, J. M., Marcos, J. L., Matía, P., Ortiz de Galisteo, J. P., Nafría, D., Fernández-González, S., Weigand, R., Hermida, L., and García-Ortega, E.: Development of tools for evaluating rainfall estimation models in real- time using the Integrated Meteorological Observation Network in Castilla y León (Spain), May 01,

509 ~~2014~~2014.

510 Mital, U., Dwivedi, D., Brown, J. B., Faybishenko, B., Painter, S. L., and Steefel, C. I.: Sequential

511 Imputation of Missing Spatio-Temporal Precipitation Data Using Random Forests, Frontiers in Water,

512 2, https://doi.org/10.3389/frwa.2020.00020, 2020.

513 Myhre, G., Alterskjær, K., Stjern, C. W., Hodnebrog, Ø., Marelle, L., Samset, B. H., Sillmann, J.,

514 Schaller, N., Fischer, E., Schulz, M., and Stohl, A.: Frequency of extreme precipitation increases

515 extensively with event rareness under global warming, Scientific Reports, 9, 16063,

516 https://doi.org/10.1038/s41598-019-52277-4, 2019.

517 Panda, K. C., Singh, R. M., Thakural, L. N., and Sahoo, D. P.: Representative grid location-multivariate

518 adaptive regression spline (RGL-MARS) algorithm for downscaling dry and wet season rainfall, J

519 Hydrol, 605, 127381, https://doi.org/10.1016/j.jhydrol.2021.127381, 2022.

520 Peng, S., Y. Ding, W. Liu, and Z. Li. 1 km monthly temperature and precipitation dataset

521 for China from 1901 to 2017. Earth Syst. Sci. Data 11:1931-1946, https://doi.org/10.5194/essd-11-

522 1931-2019, 2019.

523 Pouteau, R., Rambal, S., Ratte, J.-P., Gogé, F., Joffre, R., and Winkel, T.: Downscaling MODIS-derived

524 maps using GIS and boosted regression trees: The case of frost occurrence over the arid Andean

525 highlands of Bolivia, Remote Sens Environ, 115, 117-129, https://doi.org/10.1016/j.rse.2010.08.011,

526 2011.

527 Qin, R. and Zhang, F.: HRLT: A high-resolution (1 day, 1 km) and long-term (1961–2019) gridded

528 dataset for temperature and precipitation across China, PANGAEA [dataset],

529 https://doi.org/10.1594/PANGAEA.941329, 2022.

530 Peng, S., Y. Ding, W. Liu, and Z. Li. 1 km monthly temperature and precipitation dataset

531 for China from 1901 to 2017. Earth Syst. Sci. Data 11:1931-1946, https://doi.org/10.5194/essd-11-

532 1931-2019, 2019.

533 R Core Team: R: A Language and Environment for Statistical Computing (3.5) [code], 2018.

534 Rao, B. B., Chowdary, P. S., Sandeep, V. M., Pramod, V. P., and Rao, V. U. M.: Spatial analysis of the

535 sensitivity of wheat yields to temperature in India, Agr Forest Meteorol, 200, 192-202,

536 https://doi.org/10.1016/j.agrformet.2014.09.023, 2015.

537 Risk, C. and James, P. M. A.: Optimal Cross-Validation Strategies for Selection of Spatial Interpolation

538 Models for the Canadian Forest Fire Weather Index System, Earth and Space Science, 9,

539 e2021EA002019, https://doi.org/10.1029/2021EA002019, 2022.

540 Sadeghi, M., Nguyen, P., Naeini, M. R., Hsu, K., Braithwaite, D., and Sorooshian, S.: PERSIANN-

541 CCS-CDR, a 3-hourly 0.04° global precipitation climate data record for heavy precipitation studies, Sci

542 Data, 8, 157, https://doi.org/10.1038/s41597-021-00940-9, 2021.

543 Schamm, K., Ziese, M., Becker, A., Finger, P., Meyer-Christoffer, A., Schneider, U., Schröder, M., and

544 Stender, P.: Global gridded precipitation over land: a description of the new GPCC First Guess Daily

545 product, Earth Syst. Sci. Data, 6, 49-60, https://doi.org/10.5194/essd-6-49-2014, 2014.

546 Sekulić, A., Kilibarda, M., Protić, D., and Bajat, B.: A high-resolution daily gridded meteorological

547 dataset for Serbia made by Random Forest Spatial Interpolation, Sci Data, 8, 123,

548 https://doi.org/10.1038/s41597-021-00901-2, 2021.

549 Shi, C., Xie, Z., Qian, H., Liang, M., and Yang, X.: China land soil moisture EnKF data assimilation

550 based on satellite remote sensing data, Science China Earth Sciences, 54, 1430-1440,

551 https://doi.org/10.1007/s11430-010-4160-3, 2011.

Snell, S. E., Gopal, S., and Kaufmann, R. K.: Spatial interpolation of surface air temperatures using artificial neural networks: Evaluating their use for downscaling GCMs, Journal of Climate, 13, 886-895, https://doi.org/10.1175/1520-0442(2000)013<0886:SIOSAT>2.0.CO;2, 2000.

Tang, G., Clark, M. P., Newman, A. J., Wood, A. W., Papalexiou, S. M., Vionnet, V., and Whitfield, P. H.: SCDNA: a serially complete precipitation and temperature dataset for North America from 1979 to 2018, Earth Syst. Sci. Data, 12, 2381-2409, https://doi.org/10.5194/essd-12-2381-2020, 2020.

Tripathi, S., Srinivas, V. V., and Nanjundiah, R. S.: Downscaling of precipitation for climate change scenarios: A support vector machine approach, J Hydrol, 330, 621-640, https://doi.org/10.1016/j.jhydrol.2006.04.030, 2006.

Vapnik, V.: Principles of risk minimization for learning theory, Advances in neural information processing systems, 4, 1991.

Vapnik, V. N.: An overview of statistical learning theory, IEEE transactions on neural networks, 10, 988-999, https://doi.org/10.1109/72.788640, 1999.

Wang, B., Liu, L., O'Leary, G. J., Asseng, S., Macadam, I., Lines-Kelly, R., Yang, X., Clark, A., Crean, J., Sides, T., Xing, H., Mi, C., and Yu, Q.: Australian wheat production expected to decrease by the late 21st century, Global Change Biol, 24, 2403-2415, https://doi.org/10.1111/gcb.14034, 2018.

Webb, M. A., Hall, A., Kidd, D., and Minansy, B.: Local-scale spatial modelling for interpolating climatic temperature variables to predict agricultural plant suitability, Theor Appl Climatol, 124, 1145-1165, https://doi.org/10.1007/s00704-015-1461-7, 2016.

Xu, C., McDowell, N. G., Fisher, R. A., Wei, L., Sevanto, S., Christoffersen, B. O., Weng, E., and Middleton, R. S.: Increasing impacts of extreme droughts on vegetation productivity under climate change, Nature Climate Change, 9, 948-953, https://doi.org/10.1038/s41558-019-0630-6, 2019.

Yang, E.-G., Kim, H. M., Kim, J., and Kay, J. K.: Effect of Observation Network Design on Meteorological Forecasts of Asian Dust Events, Monthly Weather Review, 142, 4679-4695, https://doi.org/10.1175/mwr-d-14-00080.1, 2014.

Yang, K. and He, J.: China meteorological forcing dataset (1979-2018) [dataset], https://doi.org/10.11888/AtmosphericPhysics.tpe.249369.file., 2019.

Zawadzka, J., Corstanje, R., Harris, J., and Truckell, I.: Downscaling Landsat-8 land surface temperature maps in diverse urban landscapes using multivariate adaptive regression splines and very high resolution auxiliary data, International Journal of Digital Earth, 13, 899-914, https://doi.org/10.1080/17538947.2019.1593527, 2020.

Zhang, F., Zhang, W., Qi, J., and Li, F.-M.: A regional evaluation of plastic film mulching for improving crop yields on the Loess Plateau of China, Agr Forest Meteorol, 248, 458-468, https://doi.org/10.1016/j.agrformet.2017.10.030, 2018.

Zhao, Y. and Zhu, J.: Accuracy and evaluation of precipitation grid daily data sets in China in recent 50 years (in Chinese), Plateau Meteorology, 34, 50-58, https://doi.org/10.7522/j.issn.1000-0534.2013.00141, 2015.

Table 1 Summary of the accuracies for the HRLT datasets using data from the meteorological stations

Variable	MAE	RMSE	Cor	NSE	N	Period
Maximum temperature (℃)	1.07	1.62	0.99	0.98	14731830	1961–2019
Minimum temperature (℃)	1.08	1.53	0.99	0.99	14730410	1961–2019
Precipitation (mm)	1.30	4.78	0.84	0.70	14730380	1961–2019

MAE, RMSE, Cor, and NSE are the mean absolute error, root mean square error, Pearson's correlation coefficient, and Nash-Sutcliffe modeling efficiency, respectively. N is the number of observations and Period is the beginning to end years of the data.

Table 2 Comparison of accuracies for the HRLT and CMFD datasets using data from the meteorological stations

Variable	Dataset	MAE	RMSE	Cor	NSE	N	Period
Maximum temperature (℃)	HRLT	1.07	1.63	0.99	0.98	9969602	1979–2018
Minimum temperature (℃)	HRLT	1.08	1.54	0.99	0.99	9969602	1979–2018
Average temperature (℃)	CMFD	1.12	1.64	0.99	0.98	9969602	1979–2018
Precipitation (mm)	HRLT	1.30	4.73	0.84	0.71	9968784	1979–2018
	CMFD	1.30	5.85	0.75	0.55	9968784	1979–2018

MAE, RMSE, Cor, and NSE are the mean absolute error, root mean square error, Pearson's correlation coefficient, and Nash-Sutcliffe modeling efficiency, respectively. N is the number of observations and Period is the beginning to end years of the data.

Table 3 Comparison of accuracies for the HRLT and the CLDAS datasets using data from the meteorological stations

Variable	Dataset	MAE	RMSE	Cor	NSE	N	Period
Maximum	HRLT	1.10	1.73	0.99	0.98	686653	2017–2019
temperature (℃)	CLDAS	2.54	3.63	0.95	0.90	686653	2017–2019
Minimum	HRLT	1.14	1.65	0.99	0.98	686653	2017–2019
temperature (℃)	CLDAS	1.58	2.63	0.98	0.95	686653	2017–2019
Precipitation	HRLT	1.42	4.93	0.84	0.70	685936	2017–2019
(mm)	CLDAS	2.36	7.67	0.58	0.28	685936	2017–2019

MAE, RMSE, Cor, and NSE are the mean absolute error, root mean square error, Pearson's correlation coefficient, and Nash-Sutcliffe modeling efficiency, respectively. N is the number of observations and Period is the beginning to end years of the data.

Table 4 Comparison of accuracies for the HRLT and the ISIMP3a datasets using data from the meteorological stations

Variable	Dataset	MAE	RMSE	Cor	NSE	N	Period
Maximum temperature (℃)	HRLT	1.06	1.61	0.99	0.98	13973110	1961–2016
	ISIMP3a	2.47	3.47	0.96	0.91	13973110	1961–2016
Minimum temperature (℃)	HRLT	1.07	1.52	0.99	0.99	13971690	1961–2016
	ISIMP3a	2.63	3.60	0.96	0.92	13971690	1961–2016
Precipitation (mm)	HRLT	1.30	4.78	0.84	0.70	13971680	1961–2016
	ISIMP3a	2.75	8.10	0.48	0.14	13971680	1961–2016

MAE, RMSE, Cor, and NSE are the mean absolute error, root mean square error, Pearson's correlation coefficient, and Nash-Sutcliffe modeling efficiency, respectively. N is the number of observations and Period is the beginning to end years of the data.
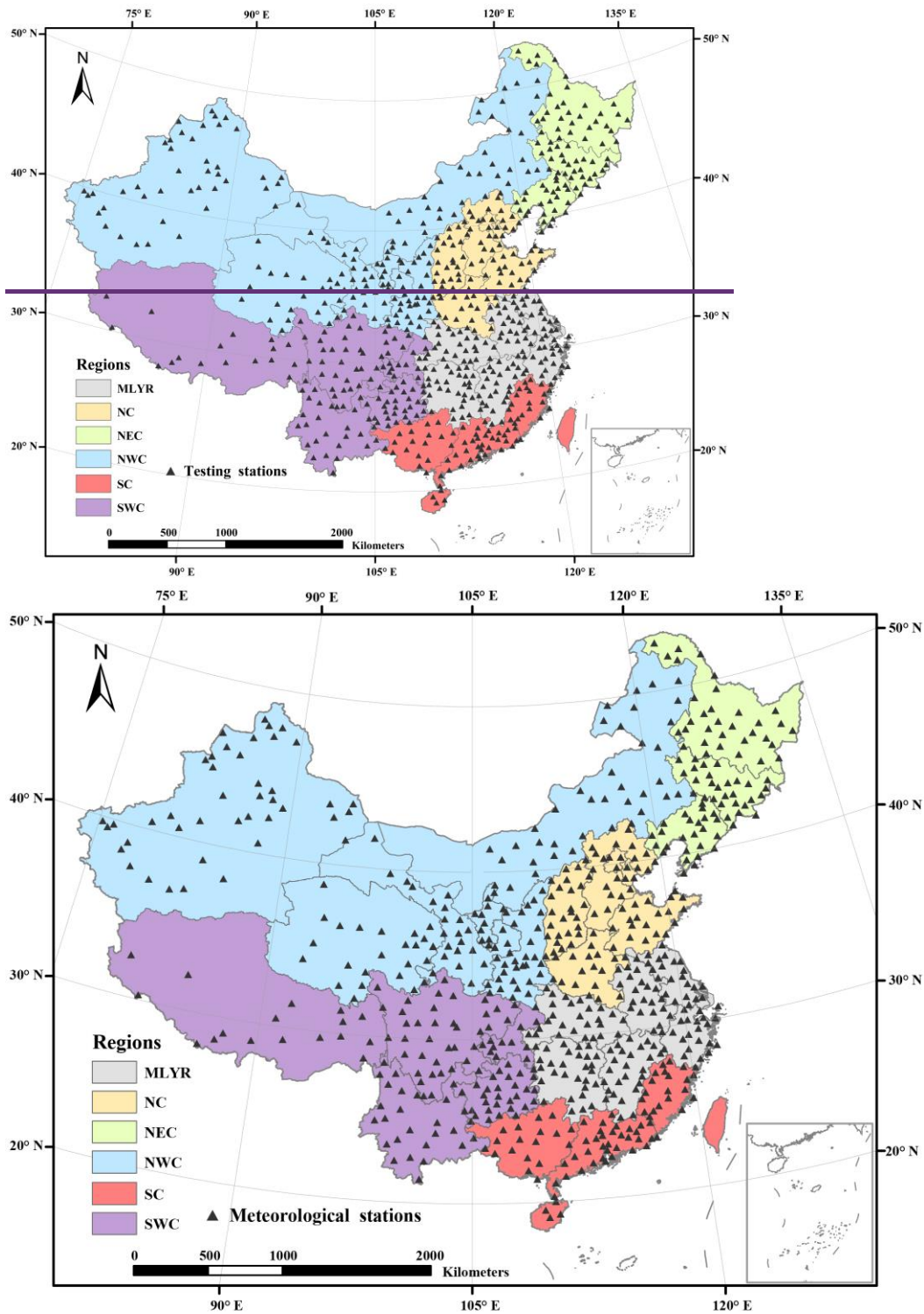
Figure 1. Regions and spatial distribution of the meteorological stations in China. MLYR, NC, NEC, NWC, SC, and SWC are the Middle and Lower reaches of the Yangtze River, North China, Northeast China, Northwest China, South China, and Southwest China, respectively. Note: meteorological stations data were missing for Taiwan Province.
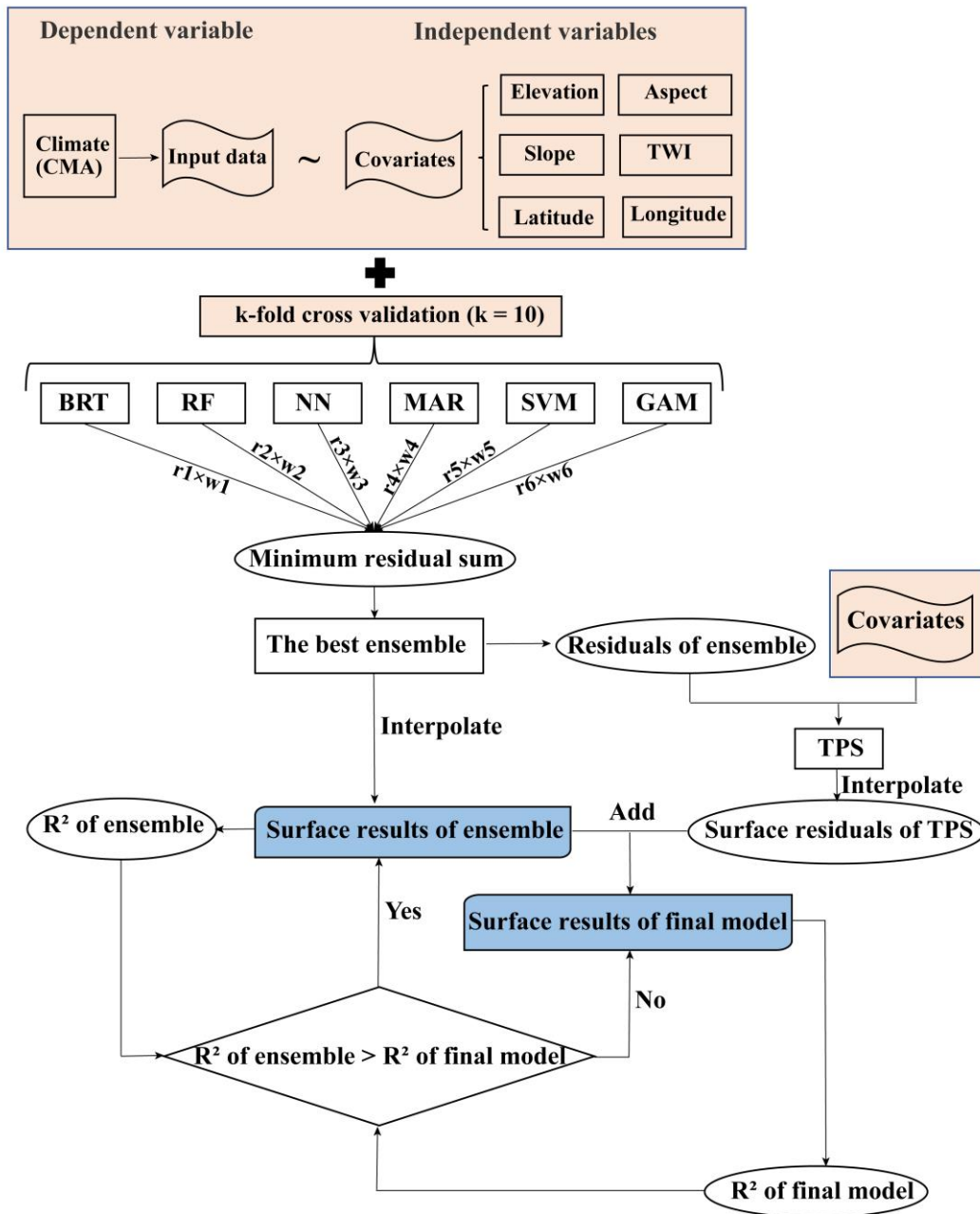
Figure 2. The process of spatial interpolation. The r1 to r6 are the residual error from each algorithm, respectively. The w1 to w6 are the weights of each algorithm, respectively. BRT, RF, NN, MAR, SVR, GAM and TPS are the boosted regression trees, random forests, neural networks, multivariate adaptive regression splines, support vector machines, the generalized additive model and thin-plate-smoothing splines, respectively. R^2 is the coefficient of determination between the estimated and observed values. **The TWI is topographic wetness index.**
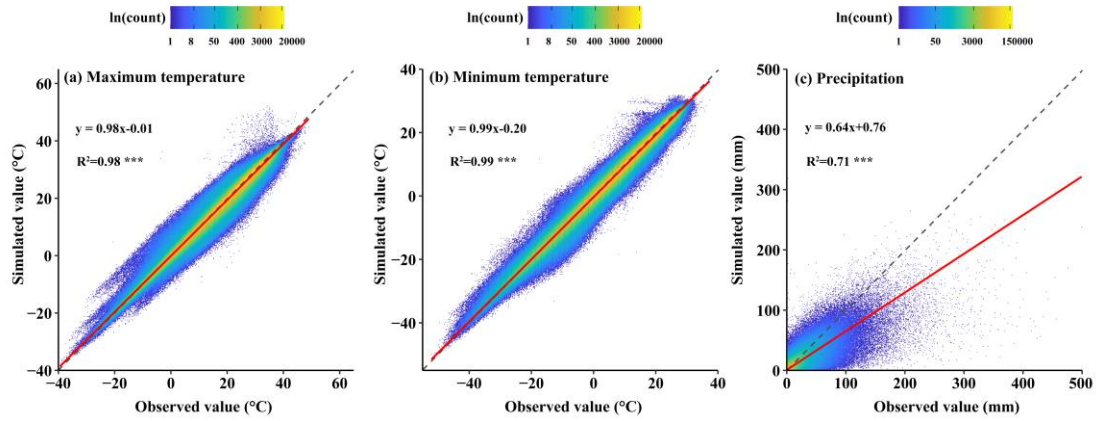
Figure 3. Scatter density plots of daily maximum and minimum temperatures and precipitation between estimated and observed values at meteorological stations were used to test the HRLT dataset. Dashed line is a line with slope 1 and the red line is a fitting between estimated and observed values. R^2 is the coefficient of determination between the estimated and observed values. *** asterisks indicate that the significance of the regression equation between the estimated and observed values was $p < 0.001$.
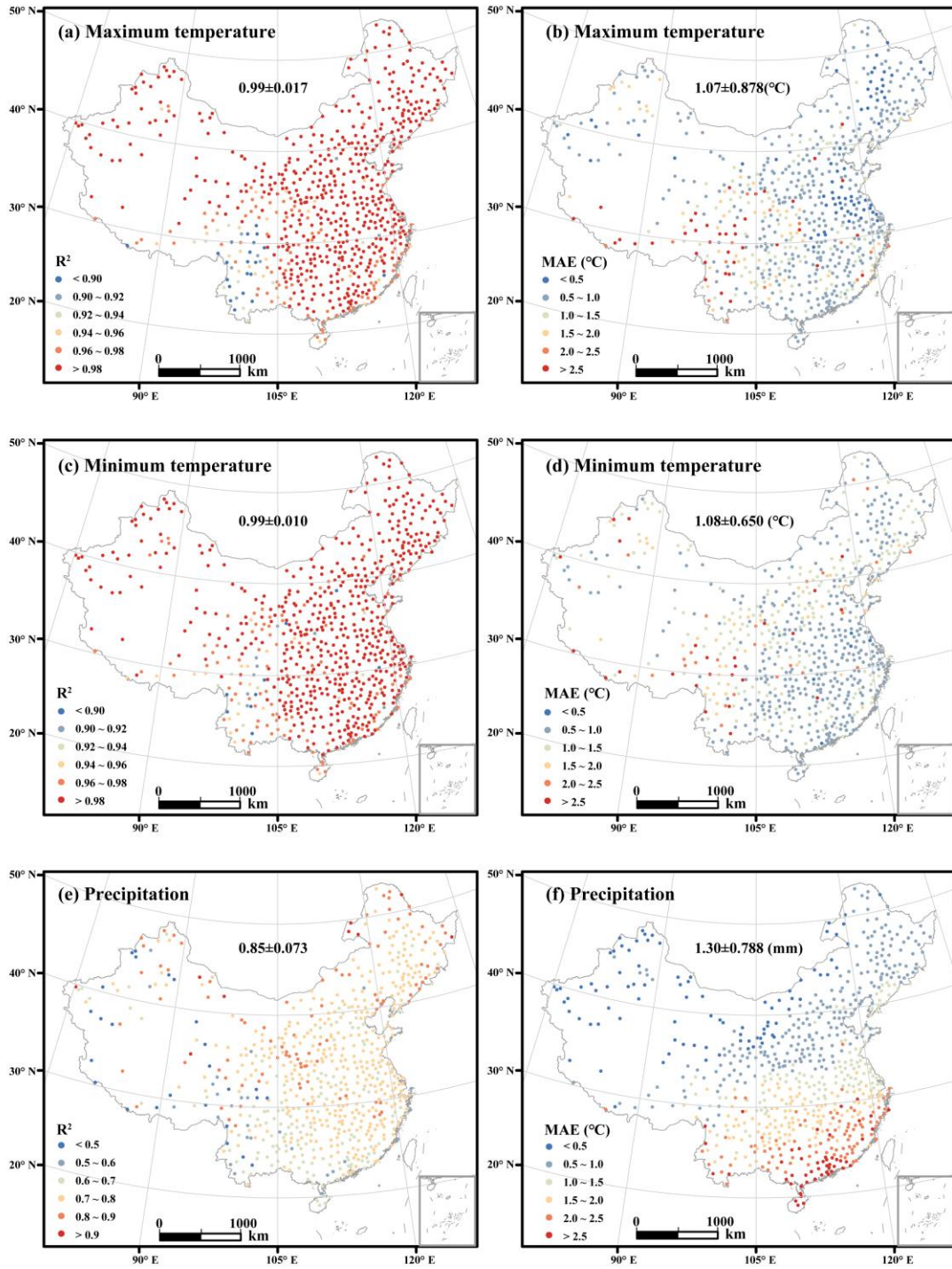
Figure 4. Spatial distribution of R^2 and MAE for daily maximum temperature, minimum temperature, and precipitation between 1961 and 2019. The value before the ± is the R^2 or MAE mean value and the value after the ± is the R^2 or MAE standard deviation for all meteorological stations.
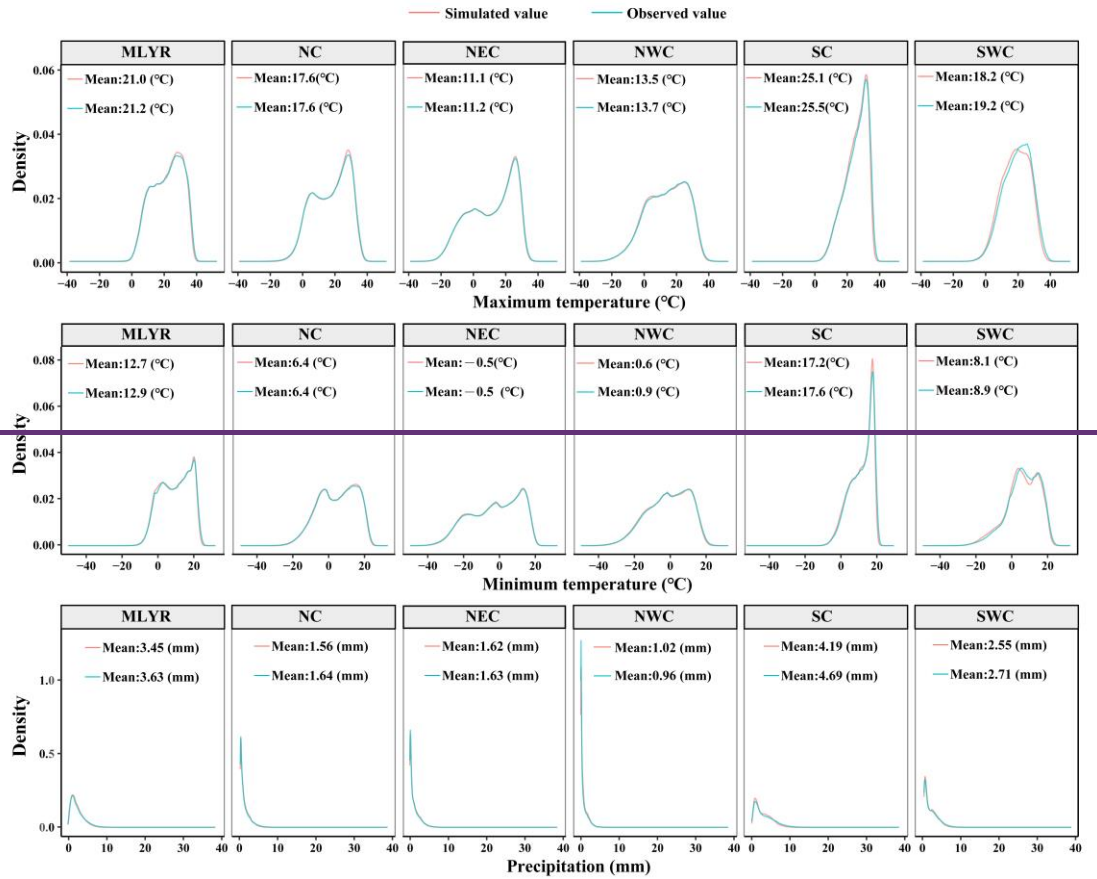
Figure 5. Comparisons of the density distribution between the estimated value in our dataset and the observed values from meteorological stations for daily maximum temperature, minimum temperature, and precipitation in the different regions from 1961 to 2019.
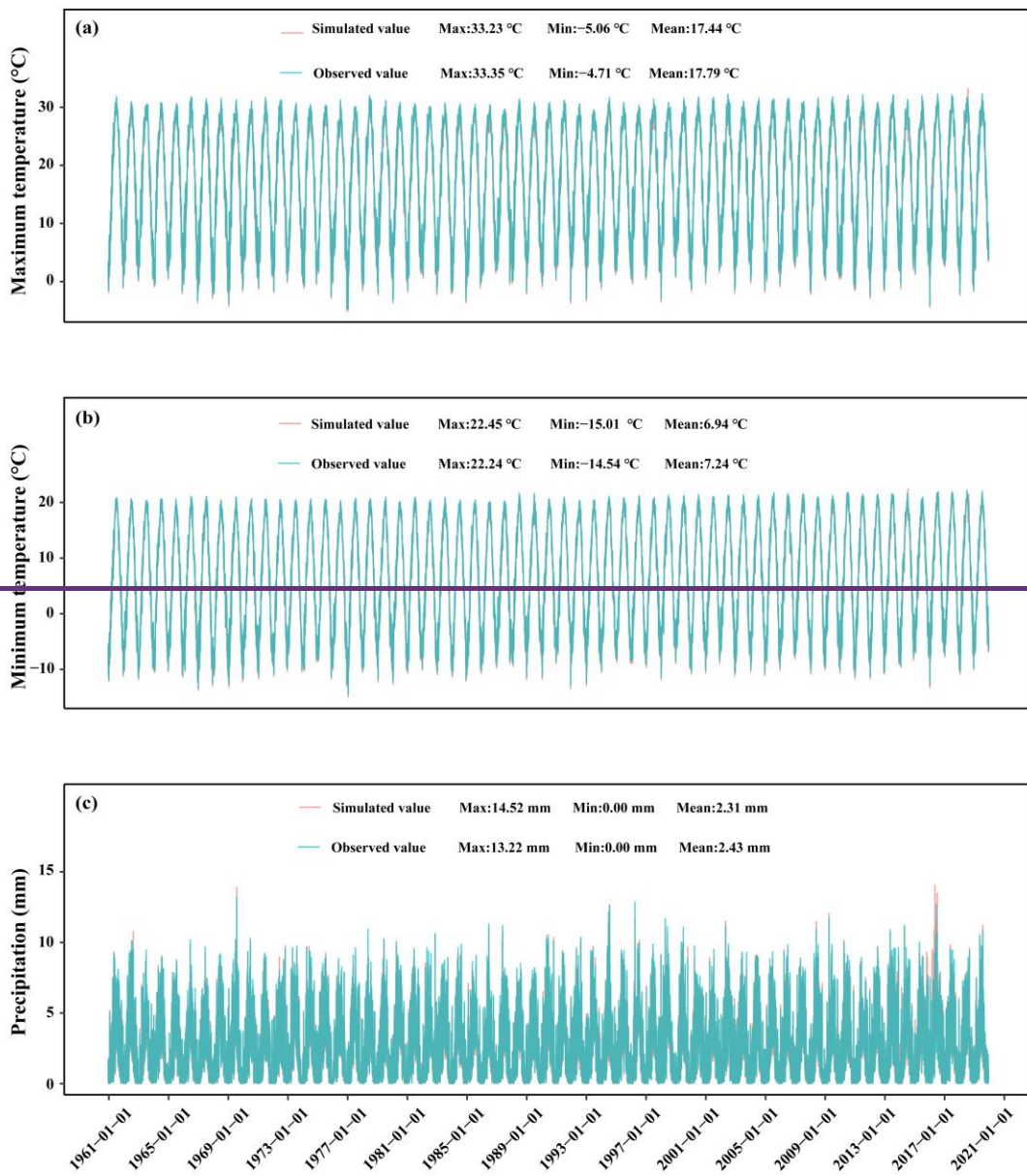
Figure 6. Comparisons of the daily changes between the estimated and observed values for daily maximum temperature, minimum temperature, and precipitation from January 1, 1961 to December 31, 2019 over all meteorological stations.
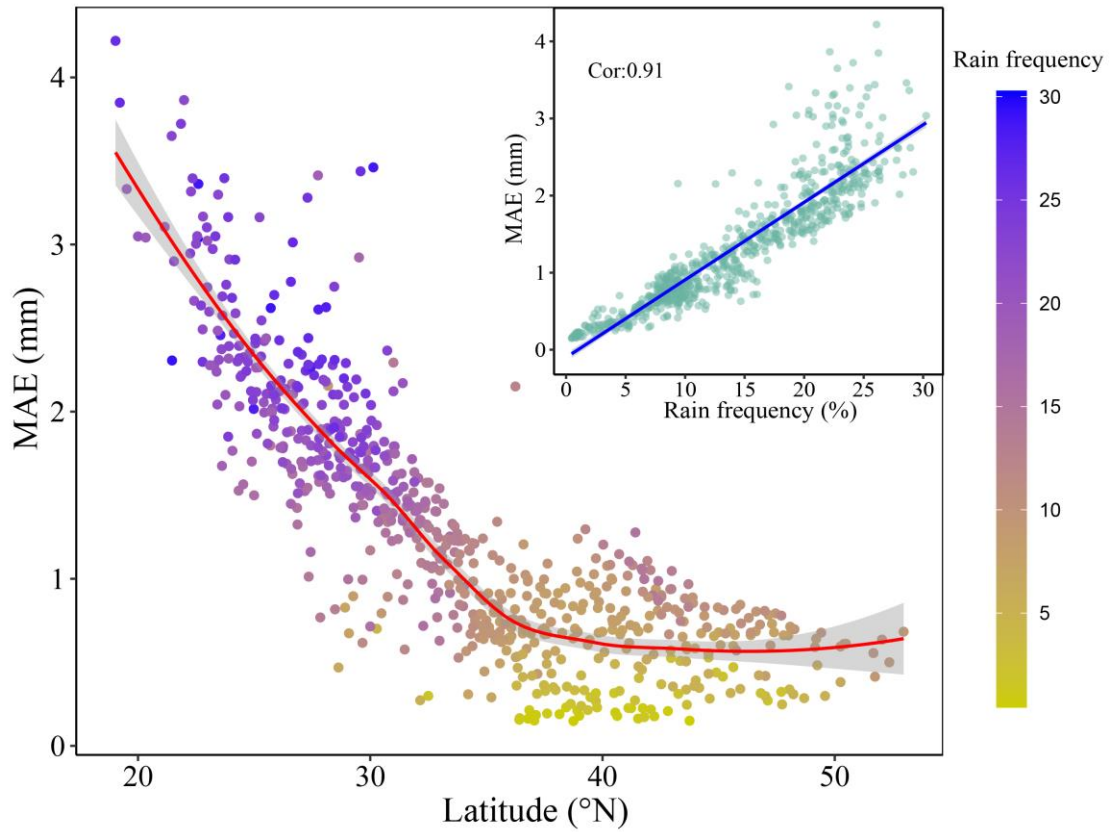
Figure 5. The relationship between latitude and MAE of daily precipitation. Illustration indicates the relationship between rainfall frequency above light rainfall and MAE of daily precipitation. MAE is the mean absolute error, Cor is Pearson's correlation coefficient, Rain frequency is rainfall frequency above light rainfall, which is defined as a daily rainfall from 0 to 4 mm (Alpert et al., 2002)
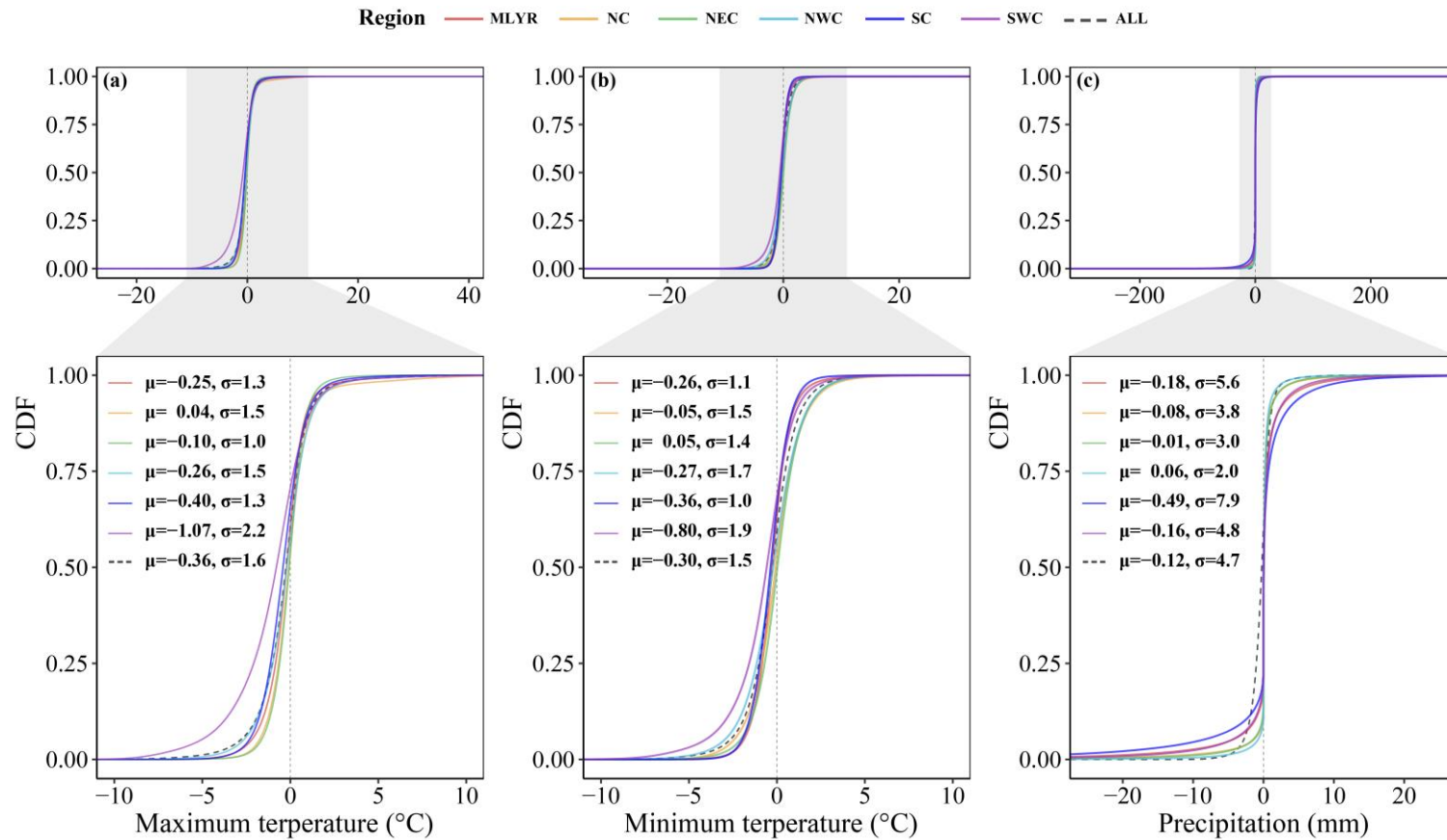
Figure 6. Cumulative distribution functions (CDF) of difference between the estimated and observed values for three variables in all meteorological stations from 1961 to 2020. μ is the mean and σ is the standard deviation. MLYR, NC, NEC, NWC, SC, and SWC are the Middle and Lower reaches of the Yangtze River, North China, Northeast China, Northwest China, South China, and Southwest China, respectively.
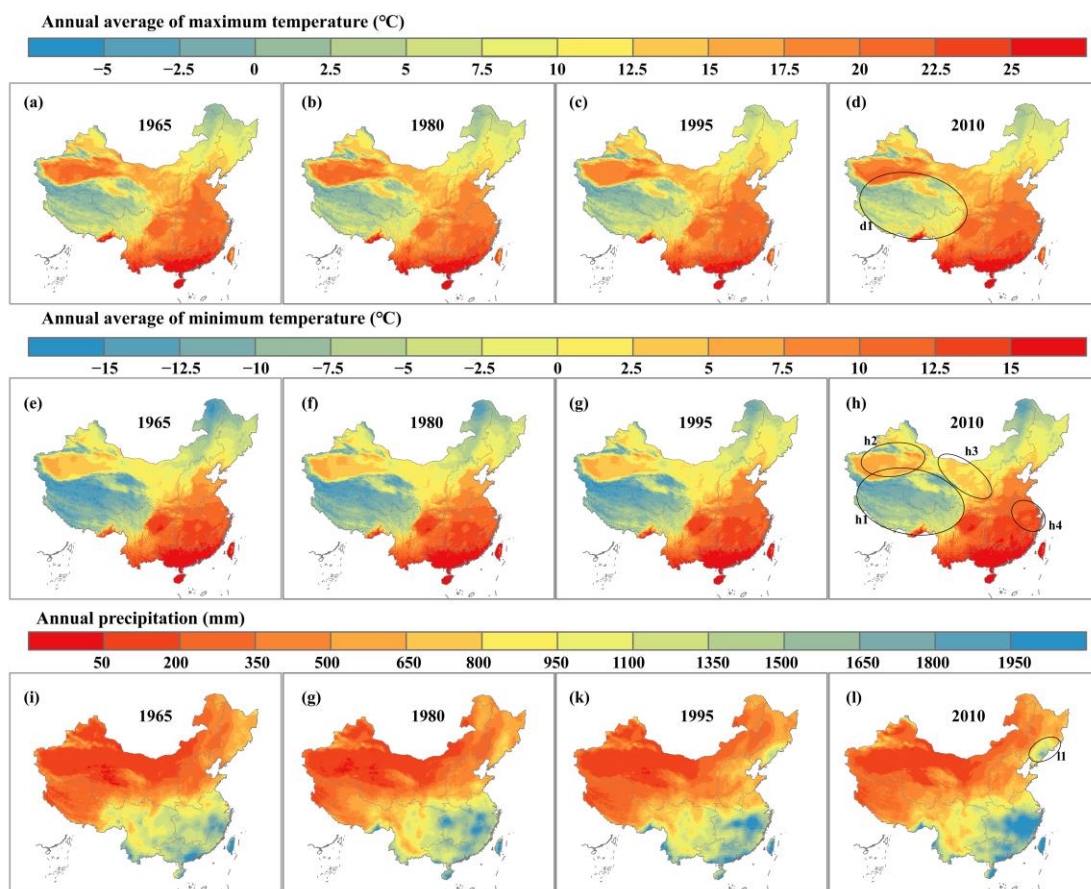
Figure 7. Spatial distributions of annual average values for daily maximum and minimum temperatures, and the spatial distribution of annual precipitation in 1965, 1980, 1990, and 2010. The ellipse regions are where the change is most visible.
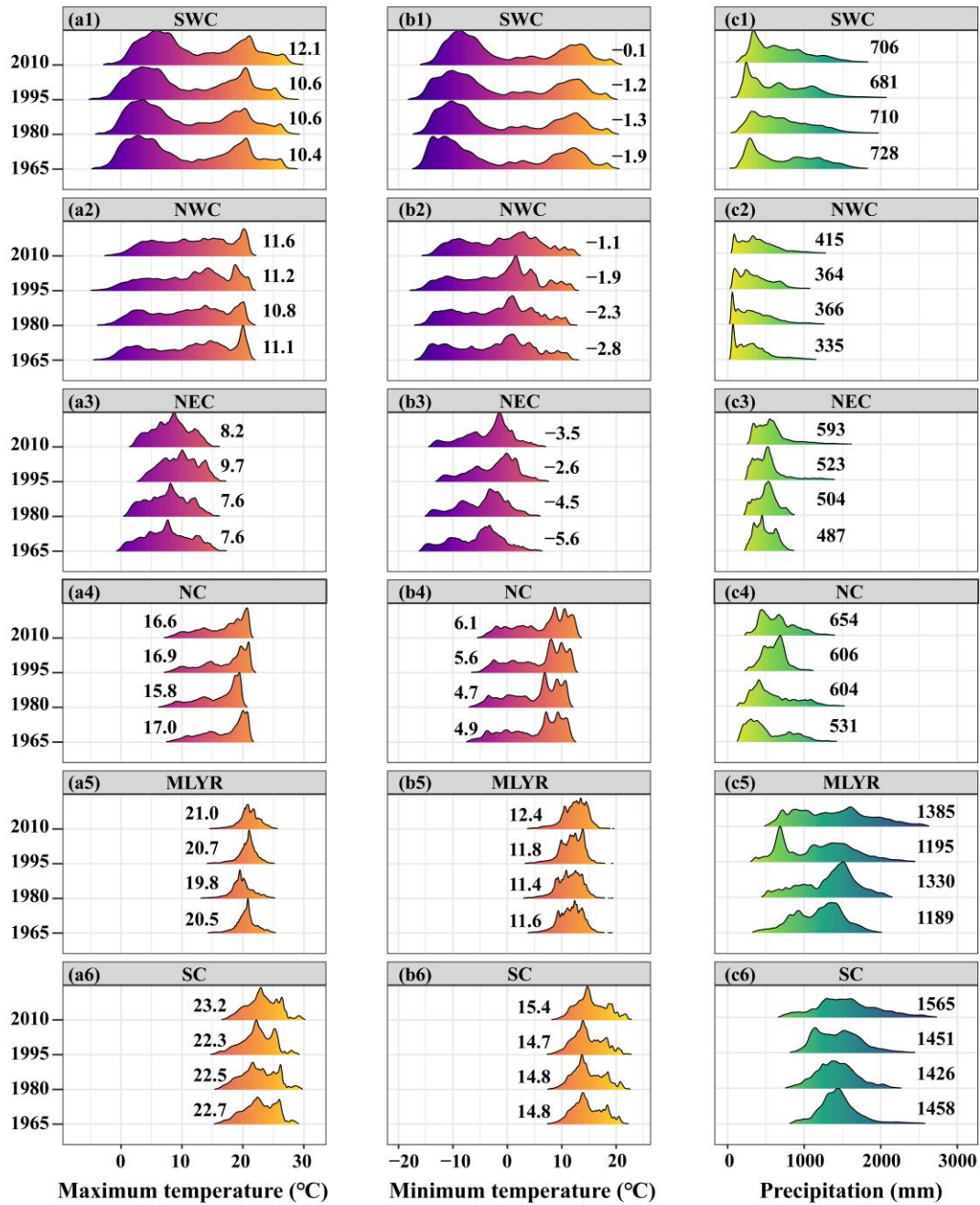
Figure 8. Density distributions of annual average values for daily maximum and minimum temperatures, and annual precipitation across the different regions in 1965, 1980, 1990, and 2010. The value in the illustrations is the mean value.
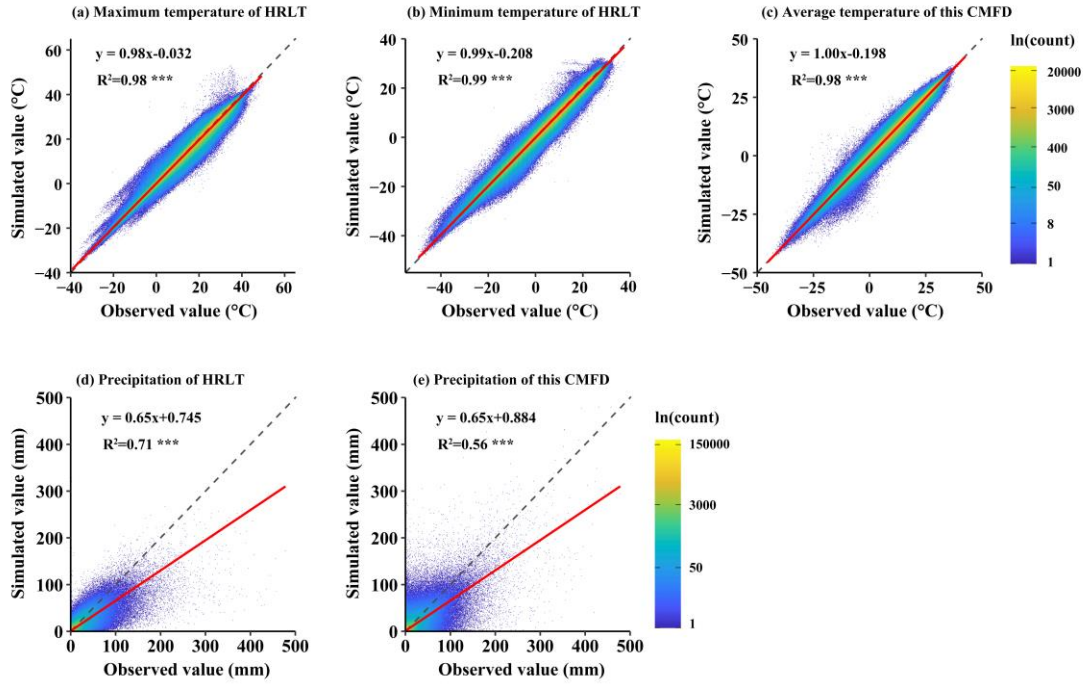
Figure 9. Scatter density plots of daily temperature and precipitation between the estimated and observed values at all meteorological stations (both training sets and testing sets) for the HRLT dataset and the CMFD dataset between 1979 and 2018. The dashed line is a line with slope 1 and the red line is a fitting between the estimated and observed values. R^2 is the coefficient of determination between the estimated and observed values. *** asterisks indicate that the significance of the regression equation between the estimated and observed values was $p < 0.001$.
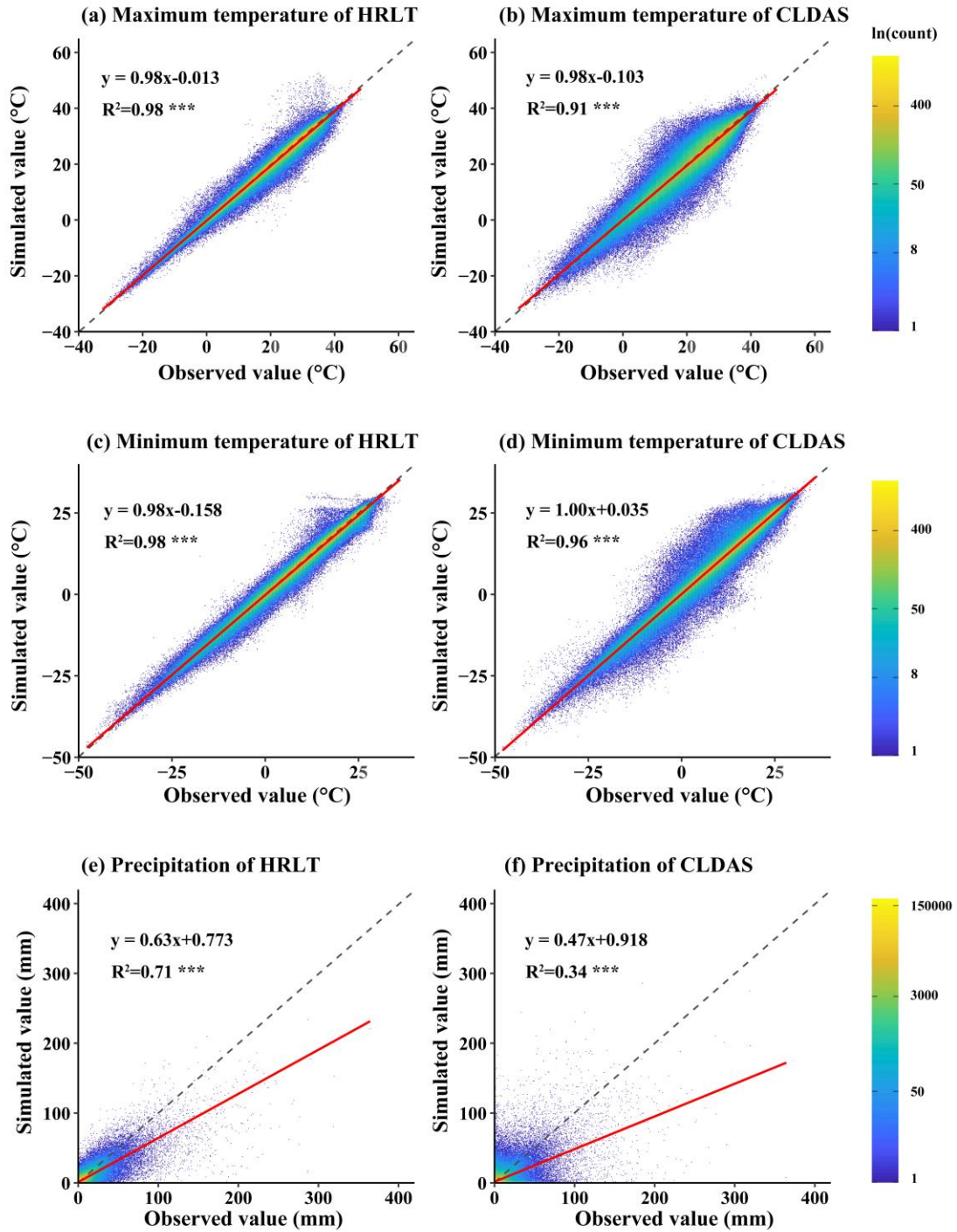
Figure 10. Scatter density plots of daily temperature and precipitation between the estimated and observed values from all meteorological stations (both training sets and testing sets) for our HRLT dataset and the CLDAS dataset between 2017 and 2019. Dashed line is a line with slope 1 and the red line is the fitting between the estimated and observed values. R^2 is the coefficient of determination between the estimated and observed values. *** asterisks indicate that the significance of the regression equation between the estimated and observed values was $p < 0.001$.
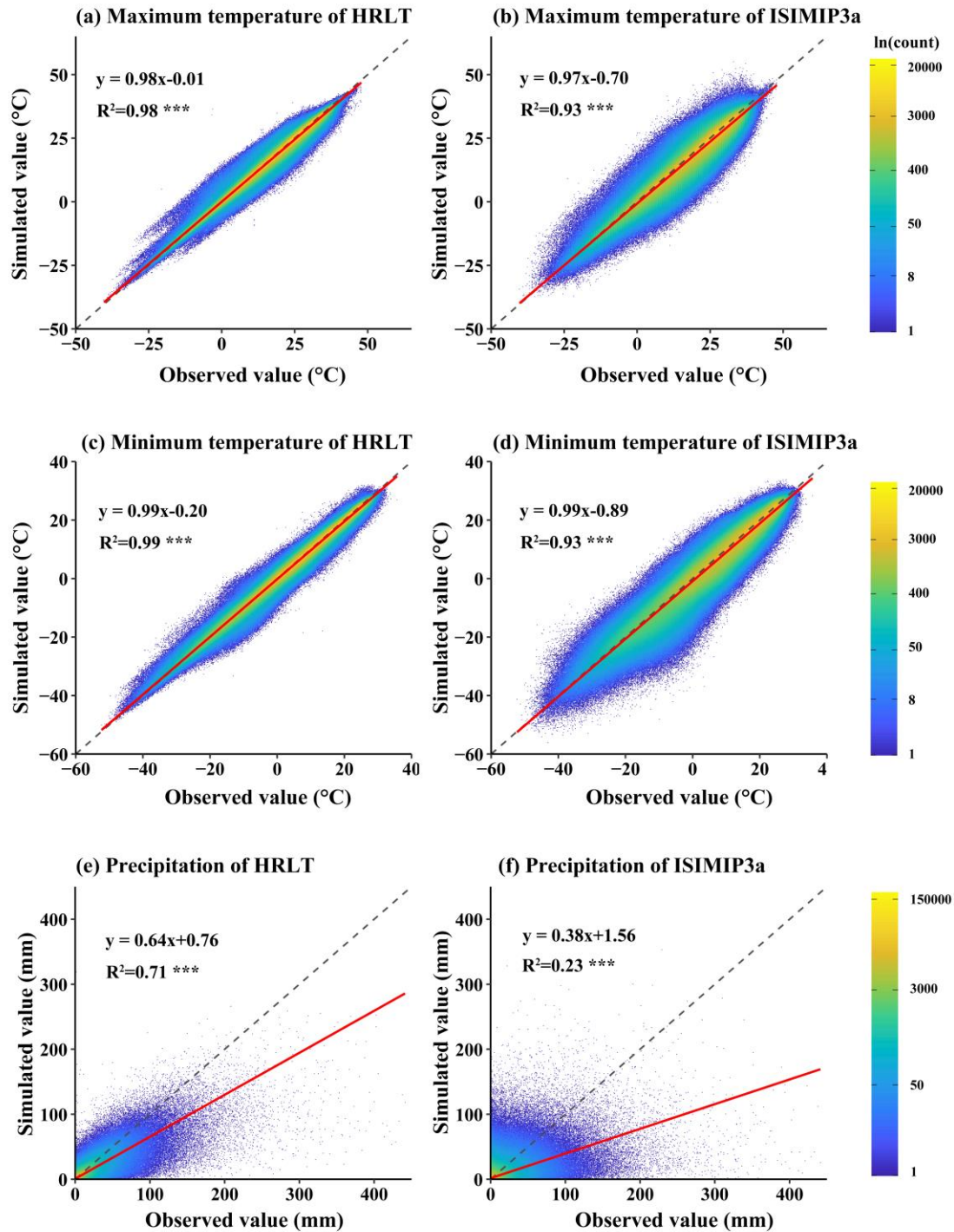
Figure 11. Scatter density plots of daily temperature and precipitation between the estimated and observed values from all meteorological stations (both training sets and testing sets) for our HRLT dataset and the ISIMIP3a dataset between 1961 and 2016. Dashed line is a line with slope 1 and the red line is the fitting between the estimated and observed values. R^2 is the coefficient of determination between the estimated and observed values. *** asterisks indicate that the significance of the regression equation between the estimated and observed values was $p < 0.001$.